Influence of Crystallographic Environment on Scandium K-Edge X-Ray Absorption Near-Edge Structure Spectra

Mathieu Chassé, Amelie Juhin, Delphine Cabaret, Steven Delhommaye, Delphine Vantelon, Georges Calas

Influence of Crystallographic Environment on Scandium *K*-Edge X-Ray Absorption Near-Edge Structure Spectra†

Mathieu Chassé,*[a] Amélie Juhin,[a] Delphine Cabaret,[a] Steven Delhommaye,[a] Delphine Vantelon,[b] and Georges Calas[a]

The absence of an extensive series of Sc *K*-edge X-ray absorption near-edge structure spectroscopy (XANES) reference spectra and the scarcity of direct structural data on Sc are major hurdles to develop our understanding of Sc chemistry. However, this first step is essential to develop new Sc-based applications and to better understand the formation of Sc deposits. Here, we present a detailed comparative study of Sc *K*-edge XANES spectra of three Sc-bearing compounds: a garnet ($Ca_3Sc_2Si_3O_{12}$), an oxide (Sc_2O_3) and a phosphate ($ScPO_4 \cdot 2H_2O$). First-principles calculations have been performed to interpret the origin of the *K* pre-edge spectral features. We demonstrate the validity of our approach by reproducing satisfyingly the experimental spectra. The densities of states projected on the absorbing Sc atom and its first neighbours give the possibility to interpret the position and intensity of the pre-edge XANES features in terms of Sc local environment. The pre-edge features provide information on *p*-*d* mixing of the absorber orbitals giving clues on the centrosymmetry of the site and on the mixing of the empty 4*p* orbitals of the absorber with empty 3*d* orbitals of the neighbours via the empty *p* orbitals of the ligands. We also show that these features give a first estimate of the crystal-field splitting energy (*ca* 1.5 eV), inaccessible using other spectroscopic methods. Comparisons with *K*-edge spectra of other $3d^0$ ions from the literature reveal the specificities of the Sc pre-edge, indicating that core-hole screening is weaker than for Ti^{4+}-bearing compounds. This study provides a dataset of spectral signatures and a theoretical basis for their interpretation, a requirement for future studies on Sc chemical form in synthetic and natural systems.

Introduction

Scandium (Sc), the lightest transition element, is one of the most elusive. Often considered as part of the rare-earth elements, as both Sc and the lanthanides occur in a trivalent state, the chemical properties of Sc differ significantly from those of other rare-earth elements[1]. This unique chemistry is exploited in high performance alloys and solid oxide fuel cells, resulting in a growing demand for this element[2]. A better understanding of the coordination chemistry of Sc is a prerequisite to developing innovative Sc-based applications[3]. In addition, the evaluation of future resources is of particular concern and requires an improved understanding of Sc speciation (*i.e.* chemical form) to trace the processes forming Sc deposits[4].

The determination of the chemical environment of Sc relies on a limited number of spectroscopic methods. With the exception of ^{45}Sc nuclear magnetic resonance (NMR) used to determine Sc speciation in crystals and glasses[5,6], Sc *K*-edge extended X-ray absorption fine structure (EXAFS) and X-ray absorption near-edge structure (XANES) spectroscopy are the only spectroscopic methods which have provided relevant information on Sc crystal chemistry. For instance, early works focused on the site distribution of Sc in synthetic garnets[7,8]. Natural Fe oxides are major phases concentrating Sc at the Earth surface and appear to be the major Sc ore in future mines. Despite low Sc concentrations that rarely exceed a few hundred parts per millions, pioneering results have been obtained thanks to the combined chemical selectivity and high sensitivity of XANES spectroscopy[4]. X-ray absorption spectroscopy has also been used to get insights into the crystal chemistry of Sc^{3+} in hydrates and aqueous solutions[3,9]. However, the absence of interpreted Sc *K*-edge XANES reference spectra[10] and the scarcity of direct structural data on Sc limit the identification of Sc speciation in complex systems[4], which explains why the coordination chemistry of Sc remains one of the most challenging topics in inorganic chemistry[3].

[a] *Institut de minéralogie, de physique des matériaux et de cosmochimie (IMPMC), Sorbonne Université, Muséum national d'Histoire naturelle, UMR CNRS 7590, IRD, F-75005 Paris, France. E-mail: mathieu.chasse@normalesup.org*

[b] *SOLEIL synchrotron, L'Orme des Merisiers, Saint-Aubin, BP 48, F-91192 Gif-sur-Yvette cedex, France*

† Electronic Supplementary Information (ESI) available: X-ray diffraction patterns, XANES spectra and demonstration of the expression of the isotropic cross section for cubic and monoclinic crystals. See DOI: 10.1039/cXCP00000x/

Except for extremely reduced environments, Sc only occurs in the trivalent state. As a consequence, Sc *K*-edge XANES spectra are of particular interest as the pre-edge region of 3*d* ions contains information on the local environment for $3d^0$ configurations[11], as the one of Sc^{3+}. Three kinds of transitions can be observed: (i) local electric quadrupole (E2) transitions $1s \rightarrow 3d$, which probe the empty 3*d* states on the absorbing atom, split by the effective crystal-field splitting (10Dq) in the presence of a 1*s* core–hole; (ii) local electric dipole (E1) transitions $1s \rightarrow 4p$, where the empty *p* states of the absorber are hybridised with its empty 3*d* states. Such a *p*–*d* mixing occurs only when the site of the absorber is not centrosymmetric, such as in tetrahedral symmetry, or if the inversion symmetry is removed by atomic vibrations[11]; (iii) non-local E1 transitions $1s \rightarrow 4p$ where the empty 4*p* orbitals of the absorber are mixed with the empty 3*d* orbitals of the nearest metallic sites via the empty *p* orbitals of the ligands[12].

This paper presents a study of high-resolution Sc *K*-edge XANES spectra, with a special attention to the pre-edge features, for three model compounds: a garnet ($Ca_3Sc_2Si_3O_{12}$, eringaite), an oxide (Sc_2O_3, scandia) and a phosphate ($ScPO_4 \cdot 2H_2O$, kolbeckite) in which the local geometry around six-fold coordinated Sc (hereafter $^{[6]}$Sc) is known. The acquisition of Sc *K*-edge XANES spectra yields a unique reference dataset, complementing previous data[4,7–9]. Spectral features have been reproduced and interpreted using density functional theory (DFT). We show the validity of this approach and demonstrate its interest to interpret the origin of pre-edge XANES features for Sc-bearing compounds in terms of coordination number, local symmetry and site distortion, orbital mixing and short- to medium-range structure. As the prevailing coordination state of Sc^{3+} is six-fold, these results not only offer new tools to interpret Sc X-ray absorption spectra but also give a basis to use first-principles calculations to determine Sc speciation in natural or synthetic systems, where Sc is incorporated at lower concentrations.

Experimental Methods

Characteristics of the Samples

Three pure Sc^{3+}-bearing compounds were used as references for this study: $Ca_3Sc_2Si_3O_{12}$, Sc_2O_3 and $ScPO_4 \cdot 2H_2O$ (Table 1). $Ca_3Sc_2Si_3O_{12}$ and Sc_2O_3 crystallise with a cubic symmetry[8,13] (space groups $Ia\bar{3}d$ and $Ia\bar{3}$, respectively) while $ScPO_4 \cdot 2H_2O$ crystallises with a monoclinic symmetry[14] (space group $P2_1/n$, Fig. 1). For the three phases, Sc atoms are six-fold coordinated with different symmetries (Table 1). In $Ca_3Sc_2Si_3O_{12}$, all Sc atoms are crystallographically equivalent in the 16*a* Wyckoff position with C_{3i} symmetry, corresponding to distorted octahedral sites, with an inversion centre and a three-fold symmetry axis. In Sc_2O_3, there are two crystallographically inequivalent Sc atoms in the 8*b* and 24*d* Wyckoff positions, with C_{3i} and C_2 symmetry, respectively. The site with C_2 symmetry corresponds to a distorted trigonal prism with a two-fold symmetry axis. In $ScPO_4 \cdot 2H_2O$, all Sc atoms are crystallographically equivalent in the 4*e* Wyckoff position, with no symmetry (C_1), corresponding to a highly distorted octahedron.

Preparation of the Samples

$Ca_3Sc_2Si_3O_{12}$. This compound was prepared following the experimental method of Bettinelli *et al.* (2011)[15] without addition of 99.99 % Eu_2O_3.

Sc_2O_3. Commercial Sigma–Aldrich Sc^{3+} oxide powder — 99.9 % trace rare earth metal basis was directly used.

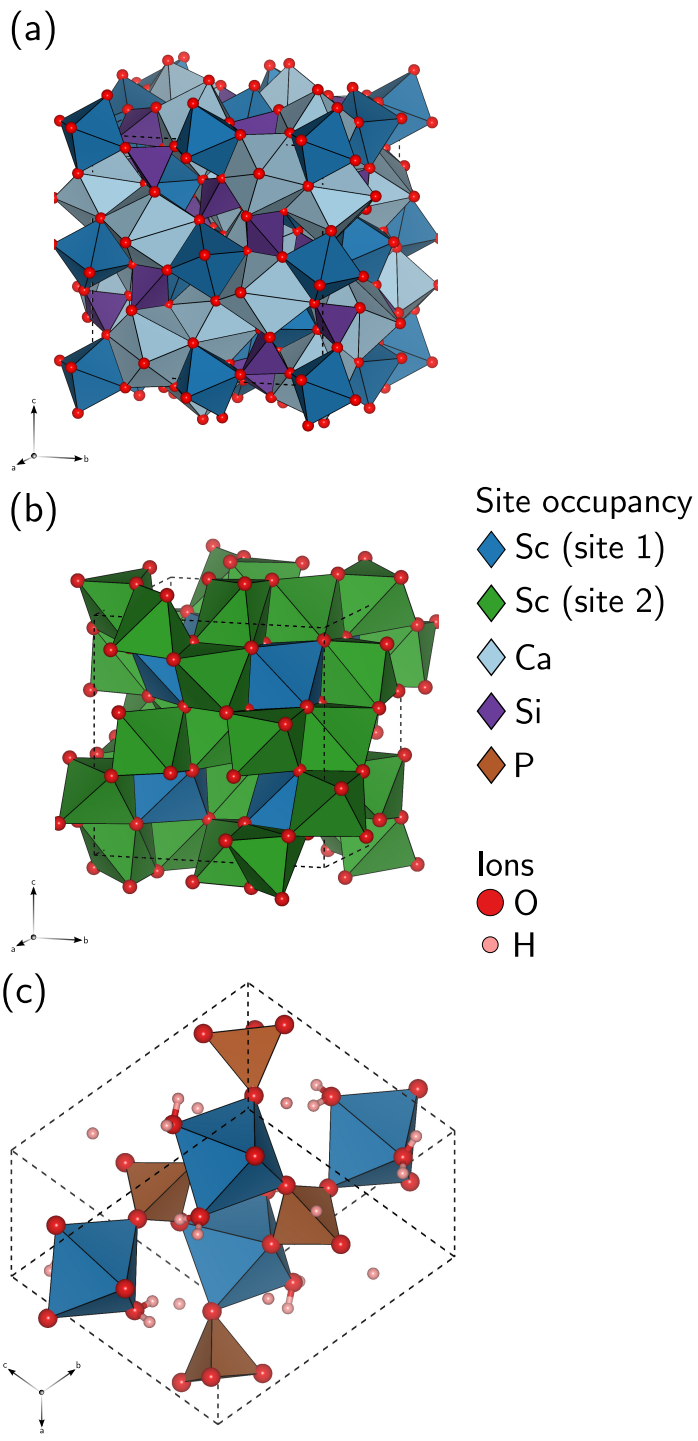

Fig. 1 Polyhedral representation of the unit cell of the compounds under study: (a) $Ca_3Sc_2Si_3O_{12}$; (b) Sc_2O_3; (c) $ScPO_4 \cdot 2H_2O$. Scandium is six-fold coordinated with C_{3i} ($Ca_3Sc_2Si_3O_4$ and site 1 of Sc_2O_3), C_2 (site 2 of Sc_2O_3) and C_1 ($ScPO_4 \cdot 2H_2O$) point-group symmetry, respectively.

Table 1 List of the compounds under study along with their crystallographic parameters and the geometric properties of the six-fold coordinated Sc sites (cryst. sys.: crystallographic system, pos.: position, abs.: absorbing, ref.: references).

Formula	Cryst. sys.	Space group	Cell parameters	Z	Wyckoff pos. (abs. atom)	Point group symmetry	Mean quadratic elongation	Bond angle variance	Ref.
$Ca_3Sc_2Si_3O_{12}$	Cubic	$Ia\bar{3}d$	a = 12.2500 Å	6	16*a*	C_{3i}	1	0	[8]
Sc_2O_3, site 1	Cubic	$Ia\bar{3}$	a = 9.8431 Å	12	8*b*	C_{3i}	1	180.5	[13]
site 2					24*d*	C_2	0.999	234.5	
$ScPO_4 \cdot 2H_2O$	Monoclinic	$P2_1/n$	a = 5.4258 Å b = 10.2027 Å c = 10.2027 Å β = 90.502 °	4	4*e*	C_1	1.001	19.1	[14]

$ScPO_4 \cdot 2H_2O$. This compound was precipitated by adding 1 g of $Na_2HPO_4 \cdot 12H_2O$ to 10 mL of 0.3 mol $\cdot$ L^{-1} $ScCl_3$. The solid product was centrifuged, washed with distilled water and dried at 45 °C for 24 h, giving 0.3 g of $ScPO_4 \cdot 2H_2O$.

Characterisation of the Samples

The crystal structures of the mineral phases have been characterised by X-ray diffraction (XRD) and the diffraction patterns are given in the ESI†. The data were collected in Bragg-Brentano geometry with a PANalytical X'Pert PRO MPD diffractometer equipped with an X'Celerator detector. Cobalt Kα radiation ($\lambda_{K\alpha 1}$ = 1.78897 Å, $\lambda_{K\alpha 2}$ = 1.79285 Å) was used. Data were recorded over the 3 °2θ to 90 °2θ range, with 0.017 °2θ steps and a total counting time of 6 h. The nature of the phases obtained was confirmed using the PDF-2 2016 database from the International Centre for Diffraction Data (ICDD, reference #00-005-0629 for Sc_2O_3) and the American Mineralogist Crystal Structure Database (AMCSD, references #0010338 for $Ca_3Sc_2Si_3O_{12}$ and #0004189 for $ScPO_4 \cdot 2H_2O$).

XANES Measurement Procedures and Data Reduction

XANES spectra at the Sc *K*-edge were collected on the LUCIA beamline[16] at the SOLEIL synchrotron in Paris (France), operating with a storage ring current of 450 mA and an energy of 2.75 GeV. XANES spectra were collected using a Si(311) double crystal monochromator. The use of such monochromators gave high spectral resolution essential for the interpretation of the pre-edge spectra, with $\Delta E/E$ of *ca* $5 \cdot 10^{-5}$. The monochromators were calibrated using the maximum intensity of the first inflection of the first derivative of Sc_2O_3 (4492.8 eV).

XANES measurements were performed in the energy range 4400 eV to 4800 eV. The energy step was (5, 0.2, 0.5 and 1) eV for energy ranges of (4400 to 4485) eV, (4485 to 4534) eV, (4534 to 4586) eV and (4586 to 4800) eV, respectively. Spectra were collected at room temperature, under vacuum, in transmission mode on pellets obtained from powdered material, diluted in a cellulose pellet and mounted on a holder between two Ultralene® films, using a photodiode. Two to five spectra were recorded for each sample with a counting time of about 10 min per spectrum.

Multiple Sc *K*-edge XANES spectra recorded for each sample were averaged before background subtraction and normalisation using the PyMCA software[17]. The pre-edge background was removed by linear fitting of the pre-edge region and subtraction from the entire spectrum. A second linear function was used to fit the post-edge region. All spectra were normalised to the edge jump using a constant corresponding to the difference between the pre-edge and post-edge fitting functions at 4505 eV. Raw spectra can be found in the ESI†.

Theoretical Approach

First-principles calculations were performed using the Quantum Espresso plane-wave based density functional theory (DFT) suite of codes[18]. Theoretical XANES spectra are obtained in two steps: (i) the charge density is obtained via self-consistent field (SCF) calculation using the PWscf code[18] and (ii) XANES spectra are computed in a continued fraction approach using the XSpectra code[19,20]. We used the generalised gradient approximation (GGA) to the exchange–correlation functional with the Perdew–Burke–Ernzerhof (PBE) parametrisation[21]. The ionic cores were described by ultrasoft pseudopotentials[22] that have been generated according to a modified Rappe–Rabe–Kaxiras–Joannopoulos scheme[23]. Scalar relativistic effects are included in the pseudopotentials. The Sc ultrasoft pseudopotential was generated considering the 3*s*, 3*p*, 4*s*, 3*d* and 4*p* states as valence states, with cut-off radii of 1.30 $\cdot$ a_0, 1.45 $\cdot$ a_0, 1.30 $\cdot$ a_0, 1.50 $\cdot$ a_0 and 1.45 $\cdot$ a_0, respectively (a_0 is the Bohr radius and $l = 2$ was taken as the local part). The pseudopotential of the absorbing Sc atom (Sc*) was generated from the Sc electronic configuration with a single 1*s* electron. The valence states of the Ca ultrasoft pseudopotential were the 3*s*, 3*p*, 4*s*, 3*d* and 4*p* states with cut-off radii of 2.30 $\cdot$ a_0 ($l = 2$ was taken as the local part). The valence states of the Si ultrasoft pseudopotential were the 3*s*, 3*p* and 3*d* states with cut-off radii of 1.80 $\cdot$ a_0 ($l = 2$ was taken as the local part). The valence states of the P ultrasoft pseudopotential were the 3*s*, 3*p* and 3*d* states with cut-off radii of 2.10 $\cdot$ a_0, 2.10 $\cdot$ a_0 and 1.90 $\cdot$ a_0. The valence states of the O ultrasoft pseudopotential were the 2*s*, 2*p*, 3*s* and 3*p* states with cut-off radii of 1.30 $\cdot$ a_0, 1.35 $\cdot$ a_0, 1.30 $\cdot$ a_0 and 1.35 $\cdot$ a_0 ($l = 2$ was taken as the local part). The valence states of the H ultrasoft pseudopotential were the 1*s* states with a cut-off radius of 0.90 $\cdot$ a_0.

Cell parameters and atomic positions used for the calculations were obtained from recently refined crystal structures of each phase[8,13,14]. Calculations were made with the 1*s* core hole successively located on each inequivalent Sc* of the cell. Due to the 1*s* core hole, the total charge of the supercell is set to +1 (full core-hole approach). $Ca_3Sc_2Si_3O_{12}$ has a cubic unit cell containing eight formula units with a = 12.25 Å. Considering the large

size of the cell, the interaction of the atom having a core hole with its periodic images is negligible and the unit cell was used directly to model this phase. Sc_2O_3 also has a cubic unit cell containing twenty formula units with a = 9.84 Å, also large enough to be used directly to model this phase. $ScPO_4 \cdot 2H_2O$ has a monoclinic unit cell containing four formula units with a = 5.43 Å, b = 10.20 Å and c = 8.91 Å (β = 90.50 °). Considering the size of the unit cell, a 2 × 1 × 2 supercell was used to model this phase. The wavefunctions and charge density were expanded in plane waves and the respective cut-offs were set from convergence tests to 85 Ry and 680 Ry. Increasing these energy cut-offs to 100 Ry and 800 Ry did not significantly modify the results. The electronic occupations were fixed. The Brillouin zone was sampled according to the Monkhorst–Pack scheme[24], using shifted 3 × 3 × 3 *k*-point grid, large enough to provide fully converged results. In order to interpret the pre-edge XANES features, partial electronic densities of states (DOS) were calculated on the systems having the core hole, using Lödwin projections, a shifted 3 × 3 × 3 Monkhorst–Pack *k*-point grid and a Gaussian broadening of 0.5 eV.

In the XSpectra code, the reconstruction of the all-electron wavefunctions is done within the projector augmented wave method[25]. To be able to treat large cells (more than one hundred atoms), the scheme uses a recursion method to construct a Lanczos basis and then computes the cross section as a continued fraction. For each compound, the absorption cross sections are calculated in the E1 and E2 approximations, on a 3 × 3 × 3 *k*-point grid, with a broadening parameter of 0.43 eV from (-10 to 5) eV relative to the Fermi level, taking into account the core-hole lifetime[26]. At higher energies, the photoelectron is fast enough to interact with the electron gas of the system and its mean free path is consequently attenuated, inducing a sharp decrease in the lifetime behavior[27]. The broadening parameter was increased accordingly up to 3 eV following an arctangent function[28] starting at 5 eV with an inflection point at 25 eV above the Fermi level.

Theoretical spectra are calculated for a given orientation of the polarisation vector and, in the electric quadrupole approximation, also of the wave vector. However, the experimental spectra are measured on powdered samples and the cross section obtained corresponds to the isotropic cross section. In order to retrieve the isotropic cross section, symmetry considerations have been used[29]. For cubic crystals, by selecting specific orientations of the polarisation and wave vectors, only one spectra needs to be calculated for the E1 approximation and two for the E2 approximation[11]. For monoclinic crystals, three spectra must be calculated in the E1 approximation and twelve in the E2 approximation. The demonstration on the number of individual theoretical spectra required to retrieve the isotropic cross sections and the corresponding orientations of the polarisation vector and the wave vector can be found in the ESI†.

In the case of Sc_2O_3, two individual spectra are obtained, one for each inequivalent Sc site. They are averaged considering the proportion of each site in the crystal structure and taking into account the core-level shift[30]. The calculated spectra are then aligned with the experimental ones with respect to the energy position of the main XANES peak.

Results and Discussion

Comparison between Theoretical and Experimental Spectra

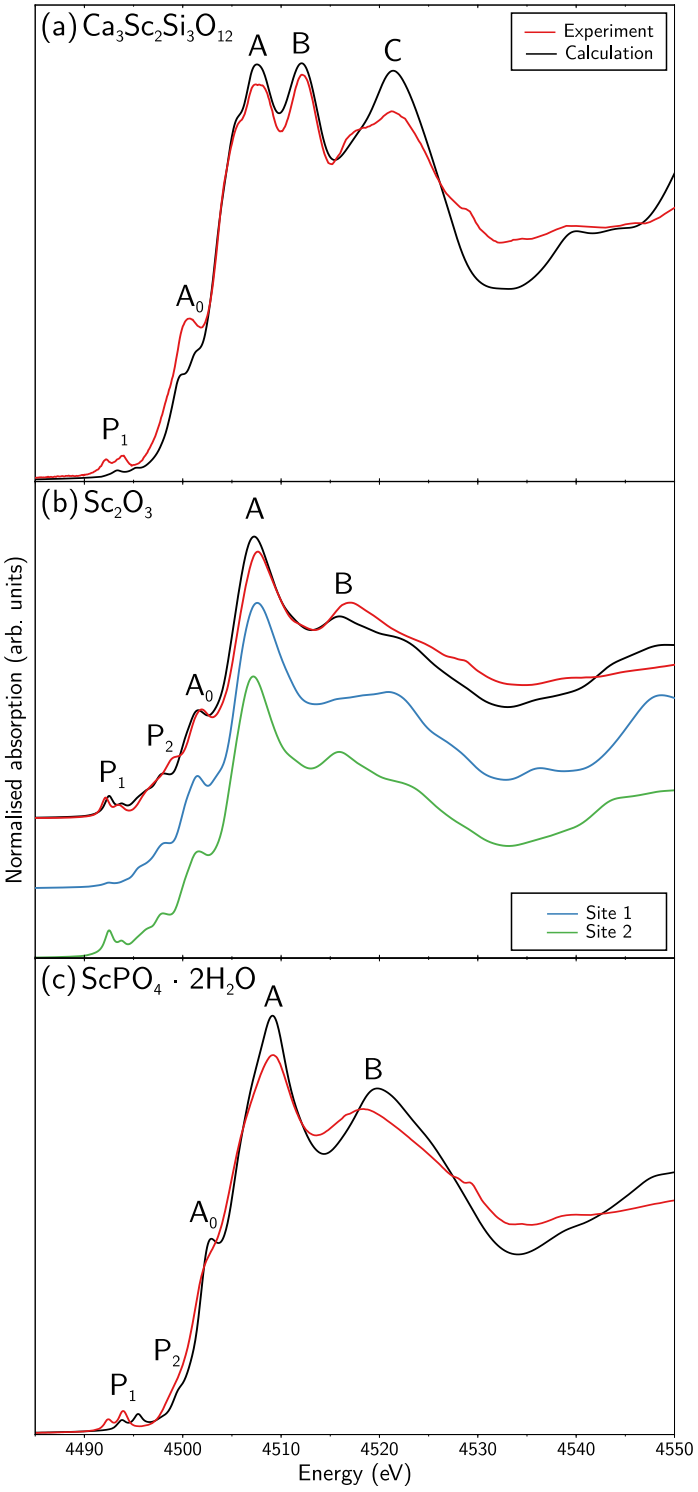

Fig. 2 Comparison between experimental (red) and calculated (black) normalised Sc *K*-edge XANES spectra for (a) $Ca_3Sc_2Si_3O_{12}$; (b) Sc_2O_3 and (c) $ScPO_4 \cdot 2H_2O$. Calculated spectra for the two inequivalent Sc sites of Sc_2O_3 (site 1 in blue and site 2 in green) are shown separately, the theoretical spectrum (red) corresponds to the sum of these two spectra weighted by the relative proportion of each site (eight sites 1 for twenty-four sites 2 in the unit cell).

Experimental Sc *K*-edge XANES spectra (Fig. 2, in red) exhibit diverse spectral features in the main edge depending on the compound considered. In the spectrum of $Ca_3Sc_2Si_3O_{12}$, three well-defined features are observed (A, B and C), respectively located at *ca* 4508 eV, *ca* 4512 eV and in the range (4516–4520) eV. They are typical of transition metal *K*-edges of calcic garnet[31–33]. The spectrum of Sc_2O_3 exhibits two main features, a sharp one (A) at *ca* 4508 eV and a broad, less intense one (B) with a maximum at *ca* 4517 eV. Two features are also observed in the spectrum of $ScPO_4 \cdot 2H_2O$, the most intense (A) being centred at *ca* 4509 eV, the second one (B) is broader with a maximum at *ca* 4519 eV. A split pre-edge feature (P_1) is observed for each spectrum in the range (4491–4495) eV. A second group of pre-edge features (P_2) is observed for the Sc_2O_3 and $ScPO_4 \cdot 2H_2O$ spectra in the range (4495–4501) eV. The energy of the P_1 pre-edge feature (centred at *ca* 4493 eV) is steady and consistent with previous works[7,9,10]. An additional feature (A_0) is visible at higher energy, *ca* 4503 eV, compared to the P_1 and P_2 pre-edge features. As discussed below, it is related to the main edge and distinct from pre-edge transitions.

The spectral variability observed in the studied compounds is reproduced in the calculated spectra (Fig. 2, in black). All major experimental features described previously are present. The position, shape and intensity are well reproduced for the A, B and C peaks in the main-edge region. The low energy pre-edge features (P_1) are shifted at higher energies in the calculated spectrum, as a result of the underestimation of the core-hole attraction on the empty *d* states of 3*d* transition metals, related to the limits of DFT[11]. However, the shape of the P_1 peaks is well reproduced, indicating our ability to explain the existence of the pre-edge features from our calculations. The relative intensity of the two P_1 features is also satisfying, the absolute intensity being only underestimated in the case of $Ca_3Sc_2Si_3O_{12}$. The P_2 and A_0 features are present with differences in terms of position and intensity.

Origin of the Pre-Edge Features

The pre-edge features contain key information on the electronic and crystallographic environments of the absorbing atom[11]. Their interpretation from calculations is not straightforward, in particular considering the complexity of the experimental spectra. To assign the transitions observed in the pre-edge spectra, the DOS for each calculated cell including the Sc 1*s* core hole have been projected on the absorbing Sc atoms and its first neighbours. We distinguish the *p*- and *d*-DOS of the absorbing Sc atom, the *p*-DOS of the first O neighbours, the *p*- and *d*-DOS of the first Ca neighbours for $Ca_3Sc_2Si_3O_{12}$, the *d*-DOS of the first Sc neighbours for Sc_2O_3 and $ScPO_4 \cdot 2H_2O$ and the *p*-DOS of the first P neighbours for $ScPO_4 \cdot 2H_2O$. For each type of neighbouring element, the projected DOS are averaged over all neighbours belonging to the same shell. In this discussion, we assume that the six-fold coordinated site of Sc is close to an ideal ScO_6 octahedron, with O_h point group symmetry. This consideration involves a crystal-field splitting of Sc 3*d* orbitals into t_{2g} and e_g orbitals.

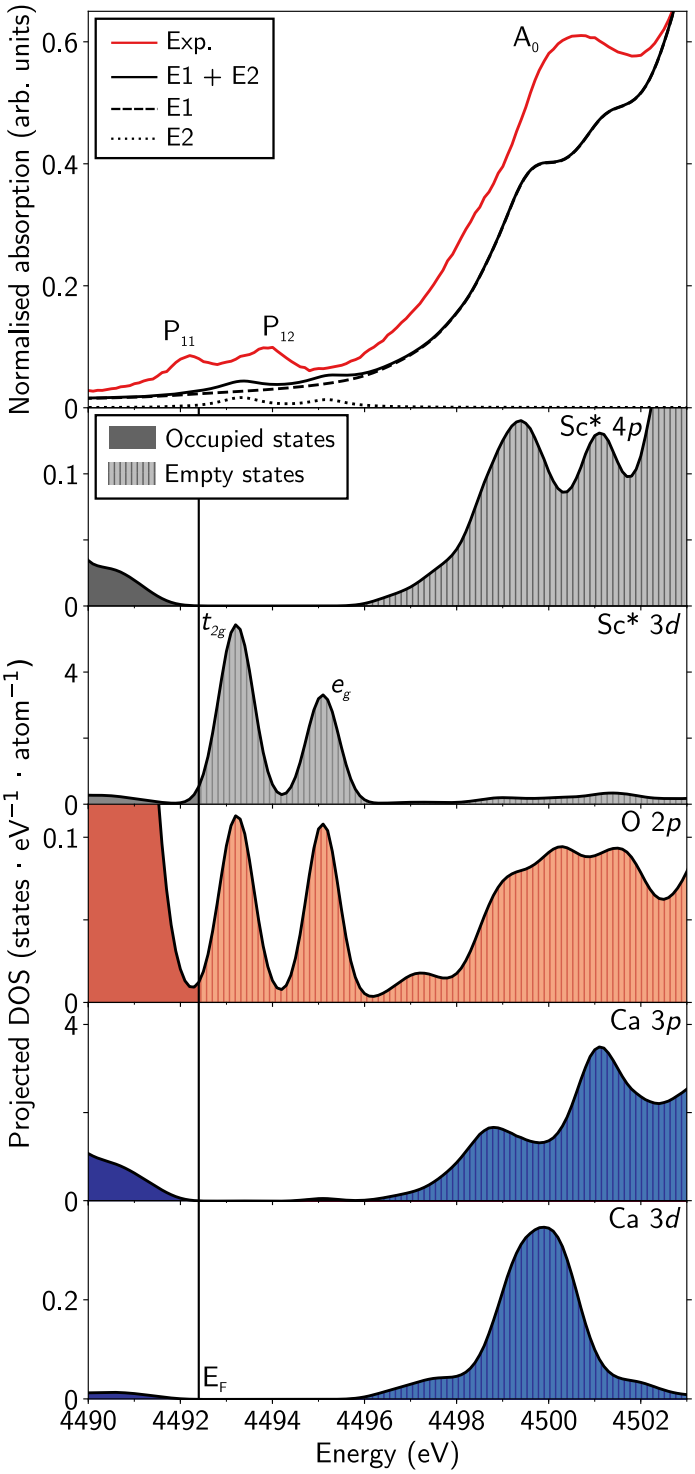

Fig. 3 Experimental and calculated pre-edge regions of Sc *K*-edge XANES spectra of $Ca_3Sc_2Si_3O_{12}$. The calculated E1 and E2 contributions have been separated. The corresponding local *p* and *d* DOS projected on the absorbing Sc (Sc*), averaged on the six 1st O neighbours and on the six 1st Ca neighbours of Sc* are shown. The vertical line (E_F) corresponds to the Fermi level. The energy scale of the projected DOS has been shifted in order to match with experimental XANES spectra.

$Ca_3Sc_2Si_3O_{12}$.

The P_1 feature, attributed to $1s \rightarrow 3d$ transitions in XANES spectra of 3*d* transition metals, is split in two (P_{11} and P_{12}) in the experi-

mental spectrum of $Ca_3Sc_2Si_3O_{12}$. Our calculations show that the P_{11} and P_{12} features are related to E2 transitions (Fig. 3). The DOS projected on the 3*d* states of the absorbing Sc atom indicate that these transitions occur from 1*s* to 3*d*–t_{2g} and 3*d*–e_g orbitals, respectively (Fig. 3 and Table 2). The calculated intensity is low, in particular when compared to the experimental pre-edge features. At the *K*-edge, the interaction between electrons and nuclear motions (*i.e.* vibronic coupling) can also enable E1 transitions to 3*s* and 3*d* final states[34]. Atomic vibrations are not taken into account by our theoretical approach but vibration-enabled E1 transitions may significantly enhance the intensity of the P_1 features[35], explaining the observed discrepancy.

The A_0 feature is related to E1 transitions but its assignment is not straightforward. The DOS projected on the absorbing Sc atom indicate that these transitions are related to the 4*p* states of the absorbing Sc, possibly indicating non-local transitions resulting from orbital mixing with the nearest metallic neighbours, via the empty 2*p* states of the O ligands. The DOS have been projected on the closest Sc neighbours, located in the third cation shell. They do not explain the A_0 feature observed. By contrast, the projected DOS indicate that orbital mixing can occur with the 3*p* of the Ca neighbour located in the first cation shell, via the O 2*p* states. However, the resulting feature is split in two in the calculated spectrum while a broad but unique feature is observed experimentally. A possible explanation may be an overestimation of the core-hole lifetime in the calculations. With increasing energy, a sharp decrease of the core-hole lifetime is induced by the interaction of the photoelectron with the electron gas of the system, attenuating its mean free path[27]. The evolution of the core-hole lifetime with increasing energy along the edge is estimated empirically[28]. With a lower core-hole lifetime, the broadening of the calculated spectrum will lead to the overlap of the A_0 features, split in our calculations. Besides, in the PBE approximation used here, the energy of the Ca orbitals can be underestimated[36]. Such an energy offset may lead to the overlap of the calculated feature of highest energy with the main edge of the spectrum.

Sc_2O_3.

The P_1 features are reproduced in the calculations for the two inequivalent sites of the absorbing Sc atoms in Sc_2O_3. The contributions from sites 1 and 2 are significantly different and Sc_2O_3 spectrum is dominated by contributions from site 2. As for $Ca_3Sc_2Si_3O_{12}$, the P_{11} and P_{12} features can be respectively assigned to E2 transitions, from 1*s* to 3*d*–t_{2g} and 3*d*–e_g states of the absorbing Sc atom (Fig. 4 and Table 2). However, the intensity of these features is also influenced by local E1 transitions. The P_{11} and, to a lesser extent, the P_{12} features are enhanced by local E1 transitions to *p* states of the absorbing Sc located in site 2 due to 4*p*—3*d*–t_{2g} hybridisation. The overall experimental P_1 features are well accounted for by these calculated transitions.

The P_2 features are also well reproduced and related to non-local E1 transitions. The projected DOS on the absorbing Sc atom indicate that these transitions can result from orbital mixing between the 3*d*–t_{2g} and 3*d*–e_g orbitals of the first Sc neighbours via the empty *p* orbitals of the O ligands, for the P_{21} and P_{22} features, respectively.

As for $Ca_3Sc_2Si_3O_{12}$, the projected DOS confirm that the A_0 feature results from E1 transitions towards the empty 4*p* states of the absorbing Sc atom and is related to the rising edge.

$ScPO_4 \cdot 2H_2O$.

As for Sc_2O_3, E2 transitions are partly responsible for the P_{11} and P_{12} features observed in the spectrum of $ScPO_4 \cdot 2H_2O$ (Fig. 5 and Table 2). These features are respectively associated to $1s \rightarrow 3d$–t_{2g} and $1s \rightarrow 3d$–e_g local transitions. The intensity of these features is enhanced by local E1 transitions due to 4*p*—3*d*–t_{2g} and 4*p*—3*d*–e_g hybridisation. The hybridisation is likely stronger with e_g orbitals, explaining why the P_{12} feature is the most intense, contrary to what would be expected from local E2 transitions. Such an hybridisation is effectively accounting for the relative intensity of the experimental P_1 features.

The low intensity and broadness of experimental P_2 feature can be related to the rising edge, blurring the details of these features along with the decreasing core-hole lifetime. However, the presence of P_2 features is reproduced theoretically and explained by non-local E1 transitions. As for Sc_2O_3, the orbital mixing of the 3*d*–t_{2g} orbitals of the neighbouring Sc atoms with the empty 4*p* states of the absorbing Sc atom via the 2*p* states of the O ligand results in a low intensity feature, P_{21} observed in the calculated spectrum but not clearly visible in the experimental one. Hybridisation with the 3*d*–e_g orbitals of the neighbouring Sc atoms explain the presence of the P_{22} feature, forming a slight feature in the experimental spectrum.

The A_0 feature likely results from the orbital mixing of the 2*p* orbitals of the neighbouring P atoms with the empty 4*p* states of the absorbing Sc atom.

Table 2 Origin of the experimental pre-edge (P) and A_0 features deduced from XANES calculations and DOS projections (neighb.: neighbour, Sc*: absorbing Sc).

Compound	Feature	Assignment
$Ca_3Sc_2Si_3O_{12}$	P_{11}	E2: $1s \rightarrow 3d$–t_{2g} of Sc*
	P_{12}	E2: $1s \rightarrow 3d$–e_g of Sc*
	A_0	E1: $1s \rightarrow 4p$ mixed with 3*p* of Ca neighb.
Sc_2O_3	P_{11}	Site 2, E1: $1s \rightarrow 4p$—$3d$–t_{2g} of Sc* + Site 1 and 2, E2: $1s \rightarrow 3d$–t_{2g} of Sc*
	P_{12}	Site 2, E1: $1s \rightarrow 4p$—$3d$–t_{2g} of Sc* + Site 1 and 2, E2: $1s \rightarrow 3d$–e_g of Sc*
	P_{21}	Site 1 and 2, E1: $1s \rightarrow 4p$ mixed with $3d$–t_{2g} of Sc neighb.
	P_{22}	Site 1 and 2, E1: $1s \rightarrow 4p$ mixed with $3d$–e_g of Sc neighb.
	A_0	E1: $1s \rightarrow 4p$
$ScPO_4 \cdot 2H_2O$	P_{11}	E1: $1s \rightarrow 4p$–t_{2g} of Sc* + E2: $1s \rightarrow 3d$–t_{2g} of Sc*
	P_{12}	E1: $1s \rightarrow 4p$–e_g of Sc* + E2: $1s \rightarrow 3d$–e_g of Sc*
	P_{21}	E1: $1s \rightarrow 4p$ mixed with $3d$–t_{2g} of Sc neighb.
	P_{22}	E1: $1s \rightarrow 4p$ mixed with $3d$–e_g of Sc neighb.
	A_0	E1: $1s \rightarrow 4p$ mixed with 2*p* of P neighb.

Insights into Electronic and Crystallographic Environments

Crystal-Field Splitting Energy.

Usually obtained by optical absorption spectroscopy, the crystal-field splitting energy, 10Dq, is only accessible through XANES spectroscopy in the case of $3d^0$ ions, such as Sc. Estimates of this pa-

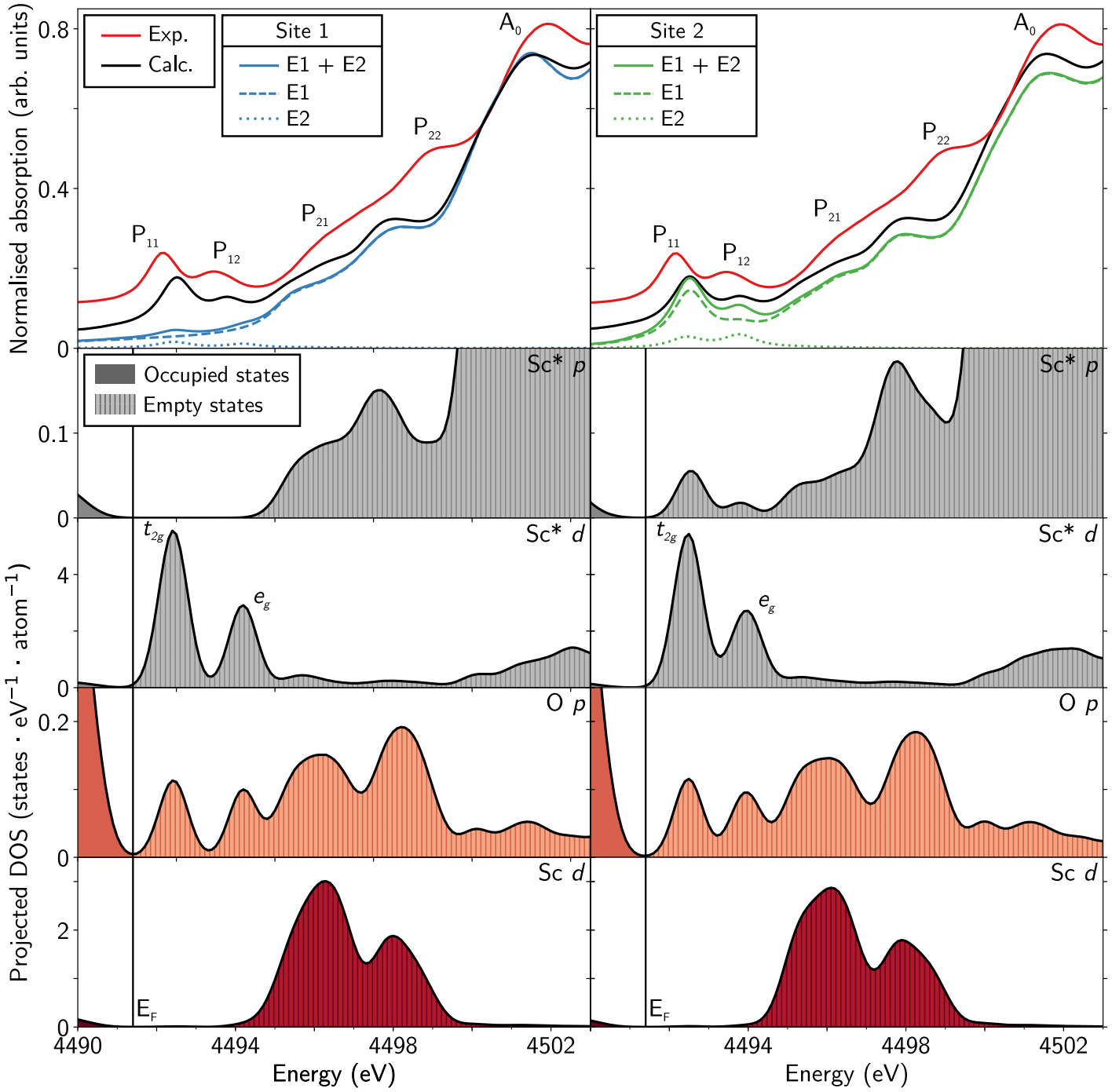

Fig. 4 Experimental and calculated pre-edge regions of Sc *K*-edge XANES spectra of Sc_2O_3. The calculated E1 and E2 contributions have been separated for the two inequivalent Sc sites. The corresponding local *p* and *d* DOS projected on the absorbing Sc (Sc*), averaged on the six 1st O neighbours of Sc* and on the twelve 1st Sc neighbours of Sc* are shown. The vertical line (E_F) corresponds to the Fermi level. The energy scale of the projected DOS has been shifted in order to match with experimental XANES spectra.

rameter are crucial to rationalise crystal field effects on transition element ions or to serve as input values in ligand-field multiplet (LFM) analyses[37]. The projection of the DOS demonstrated that the P_{11} and P_{12} features observed in the spectra of the compounds under study are related to $1s \rightarrow 3d$–t_{2g} and $1s \rightarrow 3d$–e_g transitions. The energy difference between these two features is expected to give a good approximation of 10Dq, despite the presence of the 1*s* core hole. Experimental spectra indicate 10Dq values of 1.8 eV, 1.3 eV and 1.5 eV for $Ca_3Sc_2Si_3O_{12}$, Sc_2O_3 and $ScPO_4 \cdot 2H_2O$, respectively. This value is in agreement with the value of *ca* 1.5 eV found by XANES spectroscopy for six-fold coordinated Sc^{3+} complexes in hydrated salts[9]. The crystal-field splitting energies retrieved from calculated spectra is slightly overestimated, with respective values of 1.9 eV, 1.4 eV and 1.6 eV for $Ca_3Sc_2Si_3O_{12}$, Sc_2O_3 and $ScPO_4 \cdot 2H_2O$.

The values estimated from the peak positions in the experimental

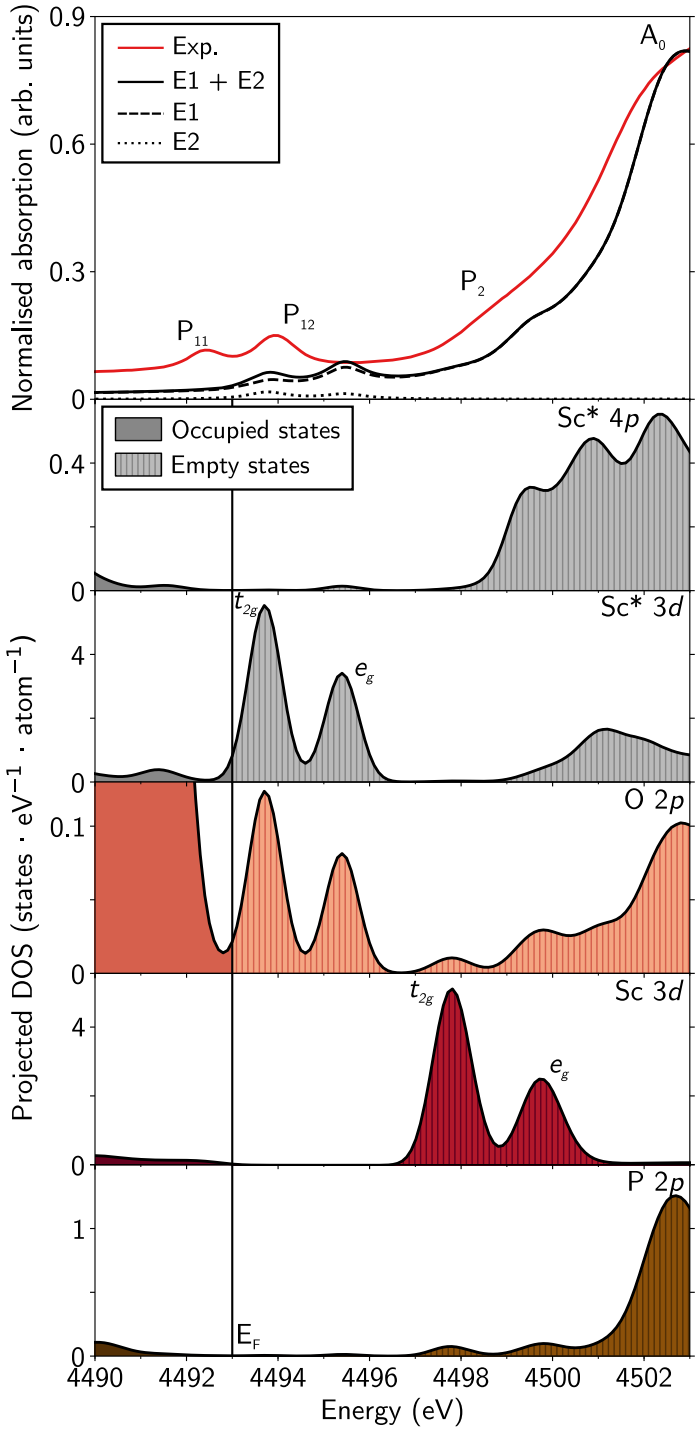

Fig. 5 Experimental and calculated pre-edge regions of Sc *K*-edge XANES spectra of $ScPO_4 \cdot 2H_2O$. The calculated E1 and E2 contributions have been separated. The corresponding local *p* and *d* DOS projected on the absorbing Sc (Sc*), averaged on the six 1st O neighbours, on the four 1st P neighbours and on the twelve 1st Sc neighbours of Sc* are shown. The vertical line (E_F) corresponds to the Fermi level. The energy scale of the projected DOS has been shifted in order to match with experimental XANES spectra.

spectra must be considered with care as these features are not always simply related to E2 transitions towards 3*d* orbitals. They can also result from E1 transitions through p–t_{2g} or p–e_g mixing or because of atomic vibrations which can slightly modify the energy of the features. The presence of two sites, as is the case for Sc_2O_3, also has an influence. The projected DOS give another estimate of 10Dq with respective values of 1.9 eV, 1.8 eV, 1.5 eV and 1.7 eV for $Ca_3Sc_2Si_3O_{12}$, the sites 1 and 2 of Sc_2O_3 and $ScPO_4 \cdot 2H_2O$. The comparison with 10Dq values obtained from calculated spectra indicate that, when orbital mixing allows E1 transitions, the 10Dq value obtained from the spectra tends to be underestimated. A rough estimation of 1.5 eV for the 10Dq value in the presence of a core hole seems consistent with experimental spectra and can be used in a first step but needs to be later refined by calculations.

The effect of the core hole on 10Dq can also be estimated from the position of the 3d–t_{2g} and 3d–e_g maxima in the DOS projected on neighbouring Sc atoms (*i.e.* with no 1*s* core hole). This crystal-field splitting energy is respectively estimated to be 2.1 eV, 2.6 eV, 2.6 eV and 2.0 eV for $Ca_3Sc_2Si_3O_{12}$, Sc_2O_3 and $ScPO_4 \cdot 2H_2O$. The presence of a core hole therefore leads to a significant underestimation of 10Dq, up to *ca* 1 eV.

Characteristics and Peculiarities of Scandium Pre-Edges.

The P_1 feature can always be related to E2 transitions from the 1*s* orbitals to 3*d* states localised on the absorbing Sc. However, the absolute intensity of the P_1 features and the relative intensity of the two components give information on orbital mixing or atomic vibrations. The intensity of the P_1 feature is enhanced by E1 transitions resulting from local p–d hybridisation of the absorbing atom orbitals (Figs. 4 and 5). This indicates the non-centrosymmetry of the site of the absorbing Sc. Atomic vibrations can induce forbidden hybridisation, as illustrated by the discrepancies observed between the experiment and the calculation for $Ca_3Sc_2Si_3O_{12}$ (Fig. 3). Local p–d hybridisation can also be highlighted by the relative intensity of the P_{11} and P_{12} components. When E1 transitions are absent, the P_{11} component is more intense than the other one, a reversal of these intensity can be observed due to a stronger p–e_g mixing compared to p–t_{2g} mixing (*e.g.* in the case of Sc_2O_3, Fig. 4).

The P_2 features result from transitions towards empty 4*p* states of the absorber, orbitally mixed with the empty 3*d* states of the first neighbours via the empty 2*p* states of the O neighbours. Calculations indicate that these P_2 features are split when they result from hybridisation with 3d–t_{2g} and 3d–e_g orbitals of the nearest metallic neighbour (*e.g.* in the case of Sc_2O_3, Fig. 4). However, the splitting of the P_2 features is not resolved experimentally when their intensity is low relative to the rising edge (*e.g.* in the case of $ScPO_4 \cdot 2H_2O$, Fig. 5).

The A_0 features are close in energy from the pre-edge features but their origin is distinct. As the main edge, they result form $1s \rightarrow 4p$ transitions, with possible orbital mixing with *p* orbitals of the nearest neighbours.

The presence of distinct P_1 and P_2 features is not common to all $3d^0$ ions. Experimental Ti *K* pre-edges of TiO_2 polymorphs (anatase and rutile), containing $^{VI}Ti^{4+}$, exhibit only three main features[38,39]. Calculations indicate however the presence of four transitions[40–43], similar to the transitions producing the P_{11}, P_{12}, P_{21} and P_{22} features observed in Sc pre-edges (Fig. 4). The E2 transition towards the 3d–e_g orbitals of the absorbing Ti

is superimposed to the E1 transition towards the *p* orbitals of the absorbing Ti mixed with the $3d$–t_{2g} of Ti neighbours. The core-hole attraction of 3*d* Sc orbitals is more important indicating a lesser core-hole screening for Sc compounds than for Ti ones. This effect is related to the nature of the chemical bonding between metal and oxygen, which may be more covalent for Sc compounds. By contrast, the presence of higher energy features, such as the A_0 feature of $Ca_3Sc_2Si_3O_{12}$, related to neighbouring alkaline-earth metals, is also identified for Ti-bearing compounds, such as $CaTiO_3$ [39] and $SrTiO_3$ [44]. Further comparison with six-fold coordinated $3d^0$ ions will require additional studies. In V^{5+}- and Cr^{6+}-bearing compounds, the metallic ion is most often tetrahedral or five-fold coordinated, prohibiting comparative analyses[45,46]. Calcium *K*-edge XANES spectra have also been published[47]. As for Sc spectra, P_1 and P_2 features seem to be present. However, the spectral resolution in the pre-edge region is limited, concealing the splitting of these features and calculated spectra are required for unequivocal assignment of the features.

In some cases, the interpretation of pre-edge features at the Sc *K*-edge is limited by the broadening resulting from the fast decaying core-hole state. Complementary information could be gained from resonant inelastic X-ray spectroscopy (RIXS). In the case of 1*s*3*p* RIXS at the Sc pre-*K*-edge, the incident photon is absorbed, promoting a 1*s* electron to the first empty 3*d* state of Sc. Then, the 1*s* core-hole is filled by a 3*p* electron accompanied by the resonant emission of a $K\alpha$ photon. The resulting high energy resolution fluorescence detection–X-ray absorption spectrum (HERFD-XAS) shows an apparent broadening which is reduced with respect to conventional XANES as it results from both 1*s* and 3*d* core-hole lifetimes[48]. In addition, as it is a two-photon resonant process, it is possible to probe both empty and occupied electronic states of the absorbing atom giving additional information on the local electronic environment of Sc, in particular when combined to LFM calculations.

Conclusions

The influence of the crystallographic environment of Sc on the spectral features observed in Sc *K*-edge XANES spectra has been studied through the experimental and theoretical characterisation of three compounds of known structure. This study provides a new set of Sc *K*-edge XANES spectra, of high interest to determine Sc speciation in natural or synthetic systems[4,10]. These successful calculations provide a theoretical basis for further first-principles calculations of Sc *K*-edge XANES spectra on poorly characterised systems. We demonstrate that such an approach is critical to interpret the observed pre-edge features. Combining experimental and calculated spectra gives access to an estimate of the crystal-field splitting energy, needed for ligand-field multiplet analysis of Sc XANES spectra[37]. Such an analysis also gives access to the local environment of Sc, informing on the degree of symmetry of the absorbing atom via the intensity of the main pre-edge features and on orbital mixing with the neighbouring atoms via low intensity spectral features present on the rising edge.

Conflicts of interest

There are no conflicts to declare.

Acknowledgements

We thank Marco Bettinelli and Roberta Oberti for providing reference samples. We acknowledge SOLEIL for provision of synchrotron radiation facilities and we would like to thank the staff of the LUCIA beamline (Proposal No. 20150692). Computer facilities were provided by GENCI–IDRIS (Projects Nos. A0020906863 and A0040906863). Mathieu Chassé has been supported by scholarships from the École normale supérieure (ENS) and Macquarie University. This work was funded by the Institut universitaire de France (IUF).

References

1 N. G. Connelly, T. Damhus, R. M. Hartshorn and A. T. Hutton, *Nomenclature of Inorganic Chemistry: IUPAC Recomendations 2005*, The Royal Society of Chemistry, Cambridge, United Kingdom, 2005, p. 377.

2 J. Emsley, *Nature Chemistry*, 2014, **6**, 1025.

3 V. Migliorati and P. D'Angelo, *Inorganic Chemistry*, 2016, **55**, 6703–6711.

4 M. Chassé, W. L. Griffin, S. Y. O'Reilly and G. Calas, *Geochemical Perspectives Letters*, 2017, **3**, 105–114.

5 N. Kim, J. F. Stebbins, S. Quartieri and R. Oberti, *American Mineralogist*, 2007, **92**, 1875–1880.

6 B. Pahari, S. Iftekhar, A. Jaworski, K. Okhotnikov, K. Jansson, B. Stevensson, J. Grins and M. Edén, *Journal of the American Ceramic Society*, 2012, **95**, 2545–2553.

7 R. Oberti, S. Quartieri, M. C. Dalconi, F. Boscherini, G. Iezzi, M. Boiocchi and S. G. Eeckhout, *American Mineralogist*, 2006, **91**, 1230–1239.

8 S. Quartieri, R. Oberti, M. Boiocchi, M. C. Dalconi, F. Boscherini, O. Safonova and A. B. Woodland, *American Mineralogist*, 2006, **91**, 1240–1248.

9 P. Lindqvist-Reis, I. Persson and M. Sandström, *Dalton Transactions*, 2006, **32**, 3868–3878.

10 S. A. Bartlett, G. Cibin, A. J. Dent, J. Evans, M. J. Hanton, G. Reid, R. Tooze and M. Tromp, *Dalton Transactions*, 2013, **42**, 2213–2223.

11 D. Cabaret, A. Bordage, A. Juhin, M. Arfaoui and É. Gaudry, *Physical Chemistry Chemical Physics*, 2010, **12**, 5619–5633.

12 A. Juhin, F. De Groot, G. Vankó, M. Calandra and C. Brouder, *Physical Review B*, 2010, **81**, 1–11.

13 J. P. S. Mowat, S. R. Miller, J. M. Griffin, V. R. Seymour, S. E. Ashbrook, S. P. Thompson, D. Fairen-Jimenez, A.-M. Banu, T. Düren and P. A. Wright, *Inorganic Chemistry*, 2011, **50**, 10844–10858.

14 H. Yang, C. Li, R. A. Jenkins, R. T. Downs and G. Costin, *Acta Crystallographica Section C: Crystal Structure Communications*, 2007, **63**, 91–92.

15 M. Bettinelli, A. Speghini, F. Piccinelli, A. N. C. Neto and O. L. Malta, *Journal of Luminescence*, 2011, **131**, 1026–1028.

16 D. Vantelon, N. Trcera, D. Roy, T. Moreno, D. Mailly, S. Guilet, E. Metchalkov, F. Delmotte, B. Lassalle, P. Lagarde and A. M. Flank, *Journal of Synchrotron Radiation*, 2016, **23**, 635–640.

17 V. A. Solé, E. Papillon, M. Cotte, P. Walter and J. Susini, *Spectrochimica Acta — Part B: Atomic Spectroscopy*, 2007, **62**, 63–68.

18 P. Giannozzi, S. Baroni, N. Bonini, M. Calandra, R. Car, C. Cavazzoni, D. Ceresoli, G. L. Chiarotti, M. Cococcioni, I. Dabo, A. Dal Corso, S. De Gironcoli, S. Fabris, G. Fratesi, R. Gebauer, U. Gerstmann, C. Gougoussis, A. Kokalj, M. Lazzeri, L. Martin-Samos, N. Marzari, F. Mauri, R. Mazzarello, S. Paolini, A. Pasquarello, L. Paulatto, C. Sbraccia, S. Scandolo, G. Sclauzero, A. P. Seitsonen, A. Smogunov, P. Umari and R. M. Wentzcovitch, *Journal of Physics: Condensed Matter*, 2009, **21**, 395502.

19 C. Gougoussis, M. Calandra, A. P. Seitsonen and F. Mauri, *Physical Review B*, 2009, **80**, 1–8.

20 M. Taillefumier, D. Cabaret, A.-M. Flank and F. Mauri, *Physical Review B*, 2002, **66**, 195107.

21 J. P. Perdew, K. Burke and M. Ernzerhof, *Physical Review Letters*, 1996, **77**, 3865–3868.

22 D. Vanderbilt, *Physical Review B*, 1990, **41**, 7892–7895.

23 A. M. Rappe, K. M. Rabe, E. Kaxiras and J. D. Joannopoulos, *Physical Review B*, 1990, **41**, 1227–1230.

24 H. J. Monkhorst and J. D. Pack, *Physical Review B*, 1976, **13**, 5188–5192.

25 P. E. Blöchl, *Physical Review B*, 1994, **50**, 17953–17979.

26 M. O. Krause and J. H. Oliver, *Journal of Physical and Chemical Reference Data*, 1979, **8**, 329–338.

27 P. Sainctavit, J. Petiau, M. Benfatto and C. R. Natoli, *Physica B: Condensed Matter*, 1989, **158**, 347–350.

28 A. Filipponi, *Journal of Physics B: Atomic, Molecular and Optical Physics*, 2000, **33**, 2835.

29 C. Brouder, *Journal of Physics: Condensed Matter*, 1990, **2**, 701–738.

30 G. Lelong, G. Radtke, L. Cormier, H. Bricha, J.-P. Rueff, J. M. Ablett, D. Cabaret, F. Gélébart and A. Shukla, *Inorganic Chemistry*, 2014, **53**, 10903–10908.

31 G. Calas and J. Petiau, *Bulletin de Minéralogie*, 1983, **106**, 33–35.

32 A. Juhin, G. Calas, D. Cabaret, L. Galoisy and J.-L. Hazemann, *American Mineralogist*, 2008, **93**, 800–805.

33 A. Bordage, C. Brouder, É. Balan, D. Cabaret, A. Juhin, M.-A. Arrio, P. Sainctavit, G. Calas and P. Glatzel, *American Mineralogist*, 2010, **95**, 1161–1171.

34 C. Brouder, D. Cabaret, A. Juhin and P. Sainctavit, *Physical Review B*, 2010, **81**, 1–6.

35 S. Nozawa, T. Iwazumi and H. Osawa, *Physical Review B*, 2005, **72**, 1–4.

36 M. Profeta, M. Benoit, F. Mauri and C. J. Pickard, *Journal of the American Chemical Society*, 2004, **126**, 12628–12635.

37 M.-A. Arrio, S. Rossano, C. Brouder, L. Galoisy and G. Calas, *Europhysics Letters*, 2000, **51**, 454–460.

38 Z. Wu, G. Ouvrard and P. Gressier, *Physical Review B*, 1997, **55**, 10382–10391.

39 F. Farges, G. E. Brown Jr. and J. J. Rehr, *Physical Review B*, 1997, **56**, 1809–1819.

40 D. Cabaret, Y. Joly, H. Renevier and C. R. Natoli, *Journal of Synchrotron Radiation*, 1999, **6**, 258–260.

41 Y. Joly, D. Cabaret, H. Renevier and C. R. Natoli, *Physical Review Letters*, 1999, **82**, 2398–2401.

42 L. D. Finkelstein, E. I. Zabolotzky, M. A. Korotin, S. N. Shamin, S. M. Butorin, E. Z. Kurmaev and J. Nordgren, *X-Ray Spectrometry*, 2002, **31**, 414–418.

43 E. L. Shirley, *Journal of Electron Spectroscopy and Related Phenomena*, 2004, **136**, 77–83.

44 D. Cabaret, B. Couzinet, A.-M. Flank, J.-P. Itié, P. Lagarde and A. Polian, *AIP Conference Proceedings*, 2007, **882**, 120–122.

45 M. L. Peterson, G. E. Brown Jr., G. A. Parks and C. L. Stein, *Geochimica et Cosmochimica Acta*, 1997, **61**, 3399–3412.

46 G. Giuli, E. Paris, J. Mungall, C. Romano and D. B. Dingwell, *American Mineralogist*, 2004, **89**, 1640–1646.

47 F. E. Sowrey, L. J. Skipper, D. M. Pickup, K. O. Drake, Z. Lin, M. E. Smith and R. J. Newport, *Physical Chemistry Chemical Physics*, 2004, **6**, 188–192.

48 P. Glatzel, M. Sikora and M. Fernández-García, *European Physical Journal: Special Topics*, 2009, **169**, 207–214.